Materials Research Bulletin 204 (2026) 114253

Contents lists available at ScienceDirect

Materials Research Bulletin

journal homepage: www.elsevier.com/locate/matresbu

Research papers

Structural, chemical and magnetic properties of pristine and Fe- doped kesterites before and after thermal annealing

Giulia Millacci [a], Alessandro Veneri [b,1], Andrea Dali [b], Alessio Gabbani [b], Beatrice Muzzi [c], Federico Spizzo [d], Arianna Rossi [d], Francesco Pineider [a], Matteo Mannini [b], Maurizio Becucci [b], Lucia Del Bianco [d], Francesco Di Benedetto [d,e,*], Lorenzo Sorace [b,**]

[a] Department of Chemistry and Industrial Chemistry University of Pisa and INSTM Research Unit of Pisa, Italy
[b] Department of Chemistry "U. Schiff", University of Florence and INSTM Research Unit of Firenze, Italy
[c] Institute of Chemistry of Organometallic Compounds, C.N.R., and INSTM Research Unit of Firenze, Italy
[d] Department of Physics and Earth Sciences, University of Ferrara, Italy
[e] INSTM Research Unit of Ferrara, Italy

ARTICLE INFO

Keywords:
Kesterites
Electron paramagnetic resonance
Magnetic measurements
Doping
Semiconductors

ABSTRACT

Here, we foster the combined use of conventional techniques to obtain a comprehensive structural and chemical characterization of kesterites (Cu_2ZnSnS_4, Copper-Zinc-Tin Sulfide, CZTS), a class of light-absorbing materials employed in sustainable thin-film solar cells, with magnetometry and Electron paramagnetic resonance (EPR) spectroscopy, to identify the nature of their paramagnetic centers. Iron-doped (CZFTS) and non-doped nanocrystals were synthesized by hot-injection method and then treated at 450°C. The structural analysis evidenced that while the raw CZTS and CZFTS nanocrystals do not show any secondary phase, a minority phase is present in the annealed samples. The complementary distribution of the metal ions in both CZTS and CZFTS was also assessed. Magnetometry and EPR spectroscopy pointed out the formation of paramagnetic vacancies following the high temperature treatment and the successful doping with Iron. This work highlighted the unique capability of a multipronged approach to detect paramagnetic defects in kesterite nanocrystals, which are otherwise challenging to identify using single techniques.

1. Introduction

In past decade, the study of materials applied in photovoltaics has been significantly expanded, with particular attention on minimizing the use of critical raw materials and toxic elements. In this context, kesterites Cu_2ZnSnS_4 (CZTS) have gained significant attention as a promising candidate for low-cost and environmentally sustainable technologies. [1–12] In particular, CZTS films produced from nanocrystals (NCs) inks offer a cost-effective solution-based method of fabrication. [13] However, the numerous routes for the synthesis of this quaternary semiconductor NCs almost invariably lead to the formation of secondary phases, antisite defects and vacancies, which reduce the efficiency of the corresponding devices. [14,15] As a contrasting action against cation disorder the replacement of Cu or Zn with other metallic elements (i.e. Ag, Cd, Fe, etc…) has been explored. [16].

In this perspective, it is crucial to obtain first a deep understanding of the types of defects and how they relate to the synthetic conditions, both in pristine and doped samples. With this aim, we decided to perform a fundamental study of both undoped (CZTS) and Fe-doped (CZFTS) kesterite NCs, before and after thermal annealing using a multitechnique approach. The structural analysis, performed by using both X-Ray Diffraction (XRD) and Raman spectroscopy, was applied to determine the phase composition of the raw synthetic and annealed samples, with a focus on the presence of possible subordinate associated phases. The overall chemical composition of the samples, as well as the distribution of the metal ions in both quaternary (CZTS) and multinary (CZFTS)

* Corresponding author at: Department of Physics and Earth Sciences, University of Ferrara, Italy.
** Corresponding author.
E-mail addresses: francesco.dibenedetto@unife.it (F. Di Benedetto), lorenzo.sorace@unifi.it (L. Sorace).
[1] currently at the Department of Computer Science, University of Verona

https://doi.org/10.1016/j.materresbull.2026.114253
Received 31 March 2026; Received in revised form 15 May 2026; Accepted 24 May 2026
Available online 28 May 2026

systems, was investigated by Energy Dispersive Spectroscopy - Scanning Transmission Electron Microscopy (EDS-STEM). The physical properties of the as-synthesized and annealed materials were verified by UV-Visible (UV-Vis) measurements, exploiting the use of Tauc plot analysis in the determination of energy band gap (E_g). Furthermore, magnetic and Electron Paramagnetic Resonance (EPR) spectroscopy analyses were applied to assess the metal valence states and to sort out the possible presence of paramagnetic defects in the samples. This multianalytical approach turned out to be very efficient in carefully tracing the defects and in evaluating the effects of thermal treatment on the magnetic and morphological properties of the CZTS lattice.

2. Materials and methods

2.1. Materials

Copper(II) acetate monohydrate ($Cu(CH_3COO)2H_2O$, Carlo Erba), Zinc(II) acetate dehydrate ($Zn(CH_3COO)_2$, ThermoScientific), Iron(II) chloride tetrahydrate ($FeCl_2{\cdot}4H_2O$, 98%, Alfa Aesar), Tin(IV) chloride pentahydrate ($SnCl_4{\cdot}5H_2O$, 98+% extra pure, Acros Organics), elemental Sulphur (S, 99.98% Aldrich) and oleylamine (OLA) (technical grade, 70%, Aldrich) were all used as received.

2.2. Synthesis

For the synthesis of the materials, we followed a procedure based on the decomposition of inorganic precursors in high boiling apolar solvents, similar to the one outlined by Y. Qu et al. [14] 0.9 mmol of Copper (II) acetate monohydrate, 0.5 mmol of Zinc(II) acetate dehydrate and 0.5 mmol of Tin(IV) chloride pentahydrate were dissolved in 25 mL of OLA preheated at 50°C in a three-neck flask connected to a Schlenk line. For the Fe-doped synthesis the amount of Zn precursor was reduced to 0.33 mmol and 0.16 mmol of Iron(II) chloride tetrahydrate were added to the reaction mixture.

The resulting solution was purged with nitrogen at 100°C for 1 h. Subsequently, the temperature was increased to 225°C, and 5 mL of a 3.6 M sulfur–OLA solution was injected. The reaction was then held at this temperature under a nitrogen atmosphere for 1 h to promote nanocrystal growth. The obtained NCs were collected after centrifugation with 1:6 toluene-acetone mixture at 7800 rpm for three times, followed by drying in air.

The annealing process was carried out with a continuous nitrogen flow inside a nitrogen-purged tube furnace maintained at atmospheric pressure. The heating rate was set to 6 °C/min and, upon reaching 450 °C, the system was held for 1 h, followed by spontaneous cooling under nitrogen atmosphere.

2.3. Experimental techniques

2.3.1. Powder X-ray diffraction patterns (PXRD)

PXRD patterns were measured in air at ambient temperature on: 1) a Bruker New D8 Da Vinci diffractometer equipped with a Bruker LYNXEYE-XE detector equipped with a Cu X- ray source (Cu Kα radiation, λ = 1.54056 Å) and 2) an Anton Paar XRDynamic 500 equipped with a Co X-ray source (Co Kα radiation, λ = 1.78021 Å). The two wavelengths were chosen to monitor the effect of the fluorescence by Fe in CZFTS samples. In all cases, data over the 2θ range 10°−80° were collected with 0.03° step size and a counting time of 1–2 s/step. Tube voltage and current were set to 40 kV and 40 mA, respectively. Data analysis, using the Rietveld algorithm, was performed using the DIFFRACT.TOPAS (Bruker) and the Fullprof suite software. [17].

2.3.2. EDS-STEM

STEM images were collected on a Thermo Scientific Talo F200X system equipped with a high brightness field emission gun (X-FEG, 80–200 keV) available at the Centro di Microscopie Elettroniche (CEME) of CNR. STEM-High-Angle Annular Dark Field (HAADF) and Bright Field (BF) images were acquired with a Panther annular STEM detector using a convergent beam with an angle of 10.5 mrad and a camera length of 330 mm. Energy Dispersive X-ray Spectroscopy (EDS) maps were taken with a Super X spectrometer equipped with four 30 mm^2 silicon drift detectors with a collection angle of 0.7 srad. Samples were prepared dispersing a small amount of NCs in toluene, then depositing few droplets of the mixture onto an ultrathin holey carbon layer film-supported Ni grid. The mean length and particle size distribution were determined through statistical analysis of more than 100 nanoparticles using ImageJ software.

2.3.3. Micro-Raman spectroscopy

Raman spectra were collected at room temperature employing a micro-Raman spectrometer RM2000 (Renishaw, Wotton-under-Edge, UK) equipped with 20×/0.40 N.A. Olympus microscope objective and a Spectra Physics model argon ion laser emitting at 514.5 nm. The microscope employs computer-controlled motorized slits allowing for a precise displacement of the sample with accuracy better than 1 μm. The spectra were calibrated on the 520 cm^{-1} first-order Raman band of bulk silicon, resulting in an accuracy within 2 cm^{-1} along the whole spectrum. A spectral resolution of 5 cm^{-1} was verified from line width measurements on the same silicon band used for calibration. To perform the measurements, a small amount of powder was put on an aluminum substrate; the laser was set to 50 μW power out of the microscope objective to avoid damaging the samples. For each sample, at least 100 individual points were registered, taking care to explore different regions in a randomized way. No relevant differences were detected within the set of data for any of the samples. The individual spectra were summed, and the analysis was carried out on the averaged data. Full profile fitting of the average spectra (obtained by summing up to 100 individual spectra) was performed using Microcal Origin 2024. The fitting included a cubic baseline function, and a set of Lorentzian peaks [18] was performed using Fityk [19] to better evaluate all the peaks. The number of the peaks was dictated by the clear identification of peaks and/or shoulders in the experimental pattern and based on data reported in the literature. [18,20,21].

2.3.4. Energy-dispersive X-ray fluorescence spectroscopy (ED-XRF)

ED-XRF was performed with a Shimadzu XRF7000 apparatus equipped with a Rh X-ray tube with a working power of 50 W (50 kV and 1000 μA) and a silicon drift detector. Software Suite PCXRF version 2.05 (Shimadzu 2018) is used for data acquisition and analysis. To perform the experiment, the samples were put in a sample cup (31.00 mm diameter × 23.10 mm height) covered with precut Mylar thin film.

2.3.5. Continuous-wave electron paramagnetic resonance (cw-EPR)

cw-EPR measurements were performed at the X-band ($\nu \sim 9.39$ GHz) on a Bruker Elexsys E500 spectrometer, equipped with either a SHQ cavity or a MD5 dielectric resonator. Low temperatures (T = 5 − 100 K) were achieved by using either an Oxford Instruments ESR900 (for SHQ cavity) or a CF935 (for MD5 resonator) continuous flow helium cryostat and an Oxford Instrument ITC503 for temperature control. All the spectra were acquired by using the same modulation frequency (100 kHz), modulation amplitude (5 G), microwave power (6 mW, 14 dB), and receiver gain (60 dB). Powder samples were placed in quartz EPR tubes (Wilmad-LabGlass 707-SQ−250 M tubes, 3 mm inner diameter). The acquired EPR spectra were exported and simulated using the open-source MATLAB toolbox EasySpin (version 6.000-dev.51) [22] and further elaborated through Microcal Origin 2024.

2.3.6. UV-visible spectroscopy measurements

Optical absorbance measurements were performed using a JASCO V−770 dual-beam spectrophotometer, equipped with a deuterium lamp (190–350 nm) and a tungsten lamp (330–3200 nm). The instrument was fitted with a 60 mm integrated sphere for diffuse reflectance

measurements on the powder samples. The spectra were collected over a wavelength range of 200–1000 nm, with a sampling interval of 0.2 nm and a scan speed of 200 nm/min. The optical E_g of the powders was determined using the Tauc plot method. This was achieved by applying the Tauc equation, which relates the optical absorption coefficient (α) to the photon energy ($h\nu$) for a material with direct band gap transition:

$$(\alpha h\nu)^2 = A(h\nu - E_g) \quad (1)$$

Here, A is a constant. Transmittance measurements were used for as-synthesized samples dispersed in C_2Cl_4. In this case we used Eq. 1 and extrapolated the band gap using the intercept of the linear fit of the linear part of the curve. For annealed samples, sinterization and irreversible aggregation make it difficult to realize stable dispersions of the NCs. Thus, such samples were analyzed only in reflectance mode. The measured reflectance spectra is transformed into absorption spectra by applying the Kubelka-Munk function:

$$F(R_\infty) = \frac{K}{S} = \frac{(1 - R_\infty)^2}{2R_\infty} \quad (2)$$

where $R_\infty = R_{sample}/R_{standard}$ is the reflectance of an infinitely thick specimen, while K and S represent the absorption and scattering coefficients, respectively. By using $F(R_\infty)$ instead of α into Eq. 1 we obtain Eq. 3:

$$(F(R_\infty)h\nu)^2 = A(h\nu - E_g) \quad (3)$$

The value of E_g was obtained by plotting $(F(R_\infty)h\nu)^2$ as a function of photon energy and extrapolating the linear portion of the curve to the x-axis, where absorption is zero.

2.3.7. Magnetometry

Magnetic measurements were performed with a Quantum Design superconductive quantum interference device (SQUID) using the Reciprocating Sample Option (RSO) mode. Polycrystalline powder samples were wrapped in Teflon and pressed in pellets to avoid preferential orientation. The specific magnetization M (i.e. the magnetic moment to sample mass ratio) was measured as a function of the magnetic field H in the 0−50 kOe range at three different temperatures (T = 1.9, 2.5 and 4.5 K) and as a function of temperature in the 2 – 300 K range at H = 10 kOe. Data were corrected both for the Teflon contribution, measured under the same experimental conditions, and for the intrinsic diamagnetic contribution of the samples estimated by using the Pascal's constants.[23].

3. Results

3.1. Structural, chemical and optical characterization of the NCs

The chemical composition of the raw and annealed samples was obtained from EDS XRF and it is shown in Table 1. The raw samples (hereafter labelled as CZTS and CZFTS, for NCs synthesized without or with Iron, respectively) reveal an overall composition consistent with the stoichiometry of the precursors. However, small but significant differences are observed, in particular in the ratio between Fe and Zn. This effect is explained in terms of the different solubilities of the two endmembers of the series (Cu_2ZnSnS_4 and Cu_2FeSnS_4[24]). Accordingly, the products exhibit the most stable composition given the thermodynamic and kinetic constraints, also considering the presence of ligands and surfactants.

One can observe a non-negligible excess of cations/sulfur ratio, but this result can be attributed to the different accuracy of the EDS measurements in the determination of X-rays from light (S) and heavier (Cu, Fe, Zn and Sn) elements. This effect is estimated in ~10% of the overall formula unit and is comparable to what already reported in literature. [25,26] Furthermore, the normalization procedure used, by which we fixed the sulfur content to 4 atoms per formula unit, propagates any uncertainty in sulfur quantification to all cationic species, leading to systematic deviations in their apparent concentrations.

The investigation of the chemical composition of the annealed samples (hereafter labelled as a-CZTS and a-CZFTS, respectively) reveals significant changes. The Sn content of a-CZTS is significantly lower than that observed in CZTS. This effect could be due to the commonly reported evaporation of SnS and SnS_2 species during the annealing. [27–29].

Fig. 1 compares the PXRD patterns of CZTS and a-CZTS samples (panel a) and CZTFS and a-CZTFS samples (panel b). If we consider the CZTS phase as belonging to $I\bar{4}2m$ space group [30] (the possible alternative choice [31] being $I\bar{4}$), some of the main diffraction peaks observed in all samples can be indexed corresponding to the (112), (200), (220) and (312) diffraction planes, respectively at 2θ values of 28.59°, 32.99°, 47.48°, and 56.30°. The patterns of the raw samples reveal significant peak broadening, linked to the small average crystallite size determined through Scherrer analysis and reported in Table 2 (estimated in 12 nm and 3–6 nm for CZTS and CZFTS, respectively). The thermal annealing of both samples led to sharper diffraction peaks, indicating improved crystallinity. Such an increase of the average crystallite size allowed for a clearer identification of the main kesterite phase in both annealed samples. Nevertheless, additional low-intensity peaks revealed the presence of a secondary phase. Even if the additional reflections are not easily discriminated from the background, we infer that this phase might be identified as herzenbergite (SnS, pertaining to the *Pmcn* space group [32]). This is consistent with the XRF results and previous literature reports, confirming that part of the original CZTS decomposes upon heating with formation of SnS.

A further insight into the structural and phase composition details of the investigated samples was obtained through Rietveld refinement (Fig. S1). The results of Quantitative Phase Analysis (QPA) indicate that the amount of herzenbergite in the a-CZTS samples is relevant (> 10 wt %, Table 2), while it is much smaller in a-CZFTS. The amount of herzenbergite in the latter case is too low, hampering a refinement of the structural parameters using QPA. In this respect, the only parameter that could be refined, namely the overall amount of SnS in association with kesterite, has to be interpreted more properly as the minimum detection limit of the analysis, given the applied experimental conditions and the intrinsic nanocrystalline nature of the investigated products. Concerning the structural details of the raw and annealed kesterites (Table 2), the comparison with the reference values suggests that in all cases a main crystalline phase with the structural features of CZTS has been obtained. Nevertheless, the raw CZFTS sample shows an apparent asymmetry of the main reflections. The best fit is obtained in this case by considering

Table 1
Chemical composition of the investigated samples from XRF data.

Label	Nominal formula coefficients					Experimental formula coefficients[a]				
	Cu	Zn	Fe	Sn	S	Cu	Zn	Fe	Sn	S
CZTS	2	1	0	1	4	2.26	1.16	0	1.20	4
a-CZTS	2	1	0	1	4	2.12	1.09	0	0.56	4
CZFTS	2	0.66	0.33	1	4	2.11	0.78	0.40	1.01	4
a-CZFTS	2	0.66	0.33	1	4	2.23	0.87	0.40	0.84	4

[a] Normalized to 4 S ions

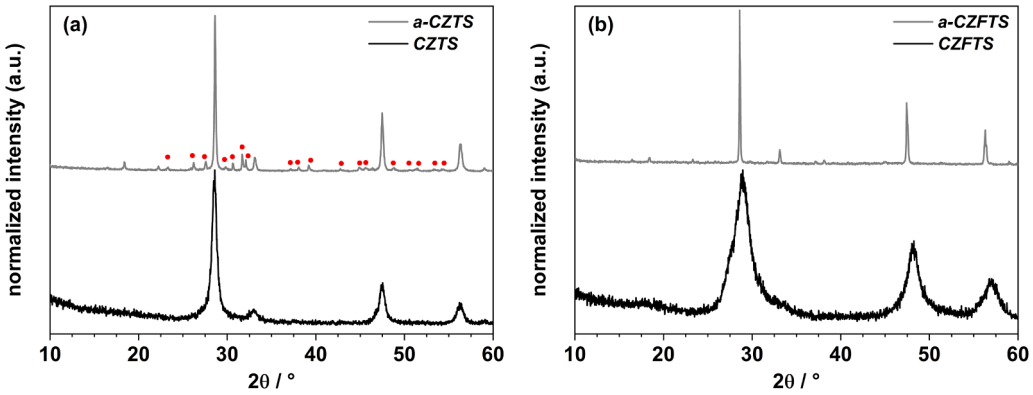

Fig. 1. Experimental PXRD of the four samples: a) CZTS (lower trace) and a-CZTS (upper trace) and b) CZFTS (lower trace) and a-CZFTS (upper trace). Red dots mark the additional reflections which cannot be indexed using the structural model of CZTS and attributed to herzenbergite.

Table 2 –
Results of the structural refinement (lattice constants) and Quantitative Phase Analysis from the Rietveld procedure and NC size from Scherrer analysis.

label		a (Å)	b (Å)	c (Å)	NC size (nm)	%
Reference	*kesterite*[a]	*5.434*	*5.434*	*10.856*		-
	herzenbergite[b]	*3.98*	*4.33*	*11.18*		-
CZTS	Phase 1	5.428(2)	5.428(2)	10.810(7)	12.4(2)	100
a-CZTS	Phase 1	5.4360(5)	5.4360(5)	10.847(1)	58.0(1)	87.6(9)
	Phase 2	3.9950(4)	4.3171(5)	11.212(1)	61(4)	12.4(3)
CZFTS	Phase 1	5.315(4)	5.315(4)	11.03(2)	3.16(2)	64(2)
	Phase 2	5.367(6)	5.367(6)	10.76(2)	6.7(1)	36(2)
a-CZFTS[c]	Phase 1	5.4257(2)	5.4257(2)	10.871(1)	137(5)	97(1)
	Phase 2	3.98*	4.33*	11.18*	79(2)	3(1)

[a] ref. [30]; [b] ref. [32]; [c] Herzenbergite was tested as associated phase, but it was not possible to refine its parameters, which are highlighted by an asterisk: the reported content represents an estimate of the detection limit under the operating conditions.

two different kesterite phases, with distinct average crystallite size (evidenced by the different linewidths of their spectral contribution) and by slight differences in the lattice parameters.

However, due to the inherent limitations of powder XRD in the determination of the phase purity, micro-Raman spectroscopy was employed for this scope. The spectra of all the samples, reported in Fig. 2, could be attributed to CZTS according to the reference standards. [18,33] Raman spectra of reference CZTS crystals are characterized by three major bands, typically reported at 265, 287 and 337 cm^{-1} (A symmetry modes). Moreover, other weaker bands are generally observed for kesterite at 252 cm^{-1} (B symmetry mode), 347 – 353 cm^{-1} (E_1 symmetry mode) and 363 – 371 cm^{-1}. [18,20,21] However, the energy and linewidth of these peaks can be significantly affected by lattice disorder, crystallite size, and impurities. [18,20,33–36] For instance, another relevant process is the known disorder-induced activation of the 332 cm^{-1} band (A symmetry mode). Table S1 summarizes the wavenumber and proposed mode assignment of the bands observed in our samples in accordance with the data reported in the literature. In particular, curve-fitting analysis (Fig. S2) evidence for raw sample (CZTS) the presence of very broad peaks at 329 and 337 cm^{-1}, while the annealed one (a-CZTS) exhibits a main resonance located at 336 cm^{-1}. The band at ~329 cm^{-1} is commonly associated with Cu–Zn cation crystallographic disorder in the CZTS structure. [18] Its disappearance after annealing indicates a reduction of this disorder, suggesting an improvement in local symmetry and cation ordering within the individual crystallites upon thermal treatment. [37].

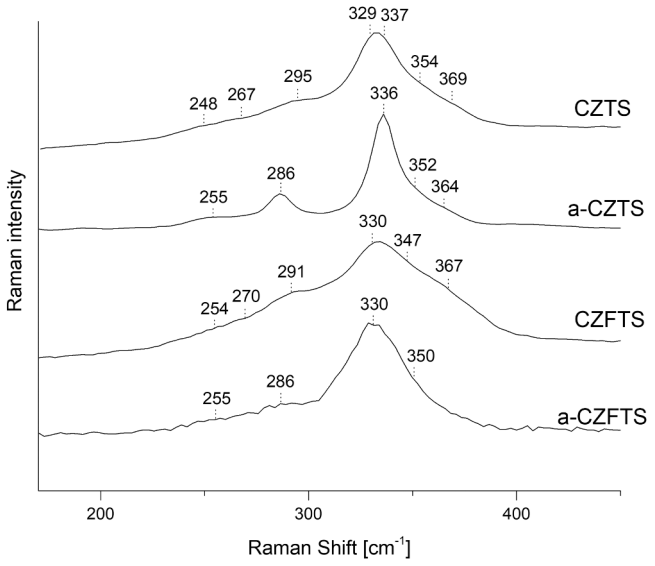

Fig. 2. Micro-Raman spectra of the different samples. The Raman shift of the most relevant peaks, identified following refs. [18] and [33] are also shown. The different contributions are deduced from the curve fitting procedure (see Fig. S2 and Table S1).

For the raw doped sample the changes with respect to the observed CZTS spectra can be discussed with reference to the work by Fontané et al. [20], who reported that in both natural and synthetic materials, for $Cu_2Zn_{0.8}Fe_{0.2}SnS_4$ chemical composition, the 337 cm^{-1} band of CZTS is shifted to 333 cm^{-1}, while for the $Cu_2Zn_{0.7}Fe_{0.3}SnS_4$ the band appeared at 330 cm^{-1}. [20] This suggests that there is a downshift trend of this band on Iron incorporation. The fit shows a band at 330 cm^{-1} for both the CZFTS and a-CZFTS (Fig. S2). The position of this band is thus compatible, at a qualitative and quantitative level, with the amount of incorporated Iron estimated by XRF.

The analysis of the full width at half maximum (FWHM) of the main 330–337 cm^{-1} peak (Table S1) combined with that of the NC size

estimated through the Scherrer analysis (Table 2) evidences that in both cases, thermal annealing (which leads to a grain size increase) results in a drastic linewidth reduction. This behavior demonstrates the effectiveness of the thermal process in the reduction of cation disorder. The Iron presence in the Fe-doped (CZFTS and a-CZFTS) kesterites is consistent with the observed larger linewidths in the Raman bands. [20].

Since both chemical and crystal phase studies suggest relevant changes in the structural organization of the NCs, an investigation on the chemical distribution of the elements in the NCs at the nanoscale was performed using EDS-STEM. The STEM image of the CZTS sample displays homogeneous nanocrystals with an average diameter of 20 ± 3 nm (Fig. 3a) This value is close to the average crystallite size revealed by XRD, thus confirming the successful synthesis of isolated CZTS NCs. EDS element mapping highlights that all the elements are present in all the regions of the NCs. However, a heterogeneous and interdependent distribution of Zn and Cu is observed, regions with low Zn content corresponding to areas of high Cu concentration. The annealed sample (Fig. 3b and Fig. S3) shows regions where Cu and Zn are more homogeneously distributed, alongside areas with Cu-rich or Zn-deficient compositions. Moreover, this sample exhibits a markedly increased particle size as well as size polydispersity (size is in the range 20–100 nm), indicating the coalescence of the NCs due to the high temperature reached in the annealing. This information, coupled with the presence of the SnS secondary phase detected through XRPD, definitely confirms that the annealing procedure, while not improving the chemical homogeneity, promotes the exsolution of phases which are thermodynamically more stable. [24].

The STEM analysis indicates that the CZFTS sample (Fig. 4a) is characterized by two primary size populations of 10 ± 2 nm and 20 ± 2 nm. When compared with the average size of the coherent structural domain revealed by XRD, this result suggests a polycrystallinity of the investigated particles. The EDS mapping shows that Fe and Zn are

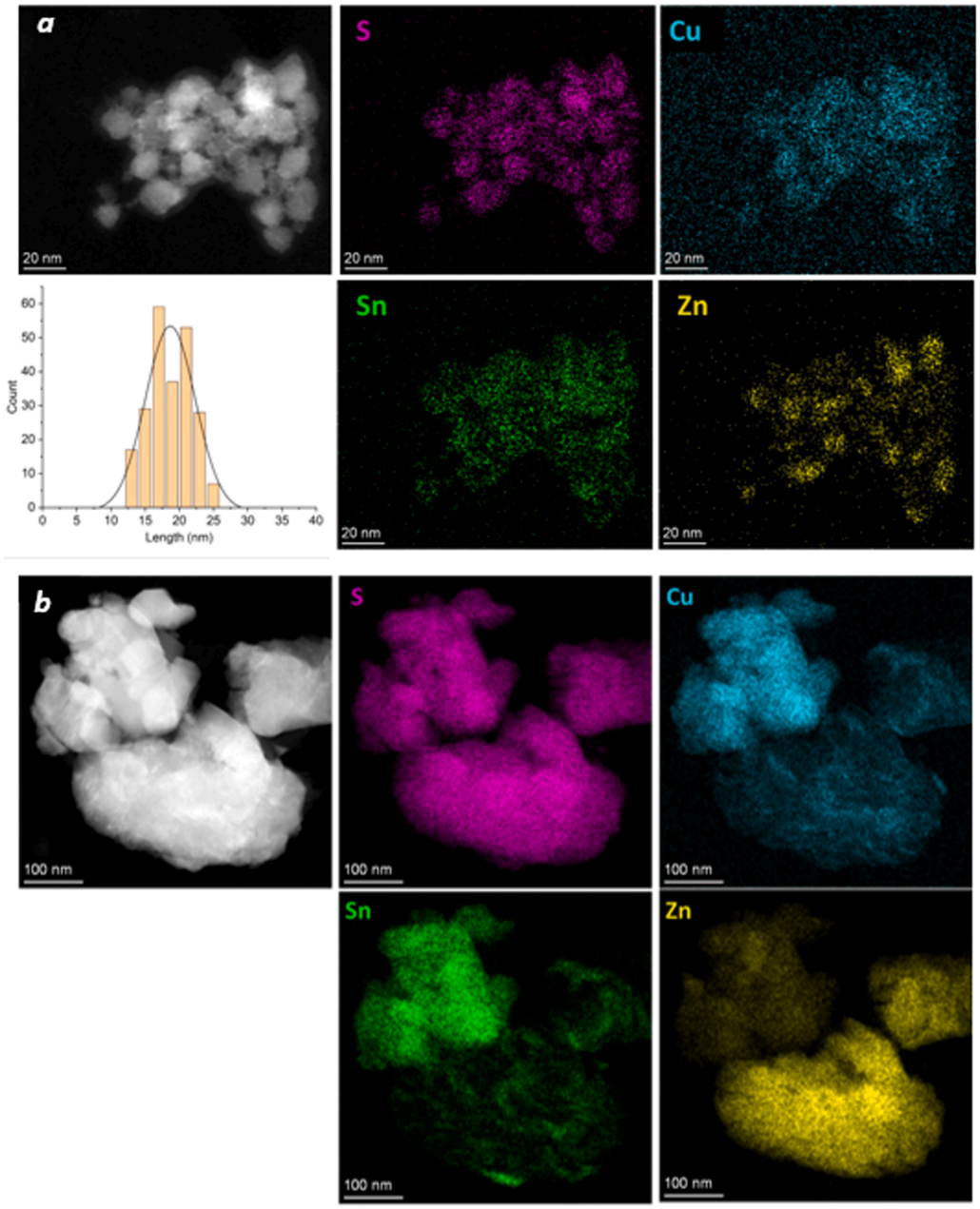

Fig. 3. STEM images of CZTS sample (a), with the size distribution fitted with gaussian function and of a-CZTS sample (b), and the corresponding EDS element mapping.

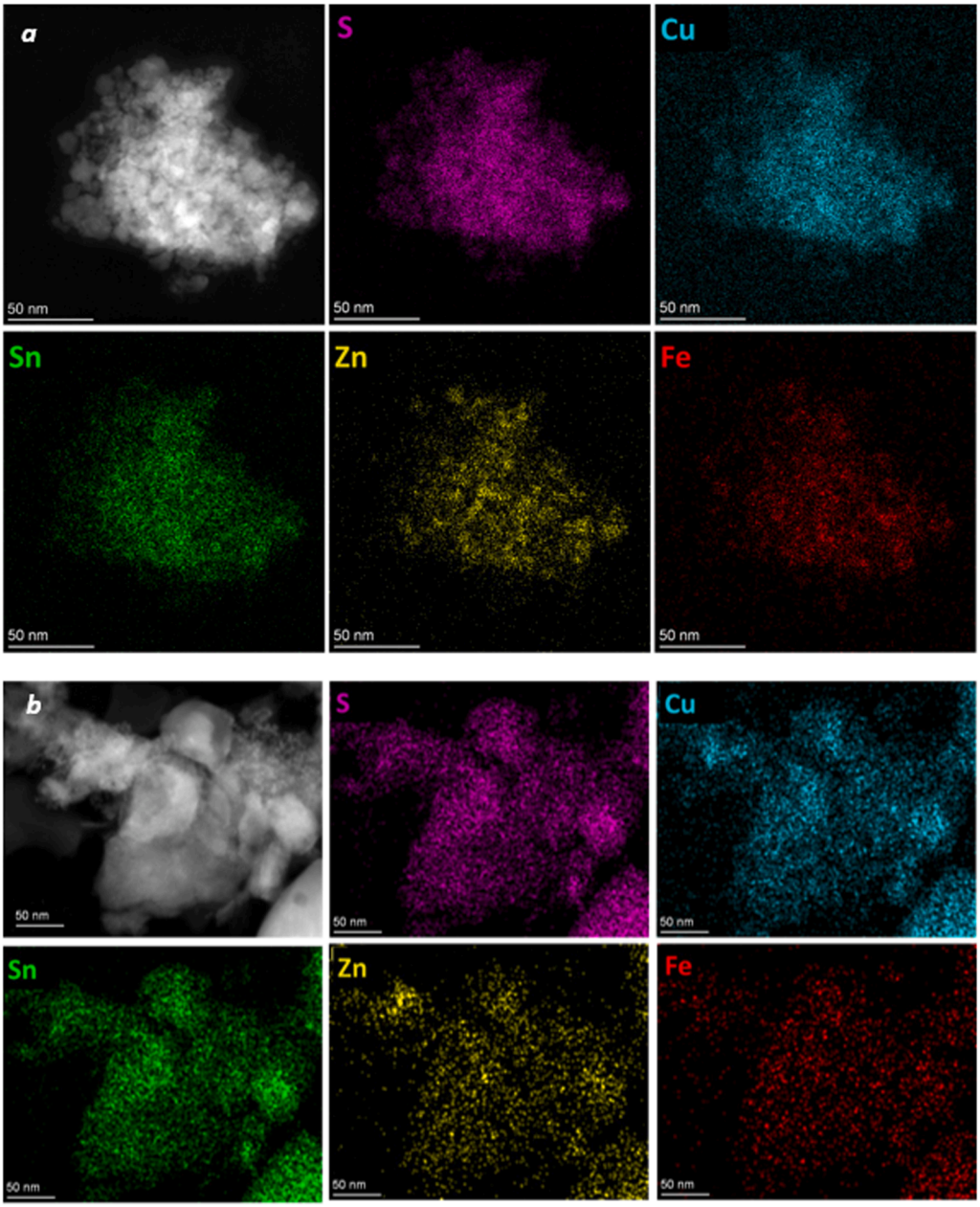

Fig. 4. STEM images of the CZFTS (a) and a-CZFTS (b) samples, and the corresponding EDS elements distribution.

almost uniformly distributed across all CZFTS particles. However, if one closely considers the single–element distribution maps of these two cations, one can easily note that several spots with high Zn intensity are present, whereas Fe exhibits a smoother distribution. Moreover, Fe exhibits an increase of concentration from the left upper corner to the center of the map, which is not paralleled by Zn or Cu. This confirms that the chemical composition of the different nanoparticles can be locally different. After thermal annealing (a-CZFTS), microscopic analysis does not reveal any significant compositional inhomogeneities or elemental segregation.

The optical properties, explored by means of the UV–Vis spectroscopy investigations, allowed to sort out optical band gaps. Optical properties of as-synthesized NCs were measured both in transmittance and in reflectance mode (Fig. S4 in Supporting Information file), yielding comparable results (Table S2) when considering the experimental error and the complexity of the system. Indeed, point defects are typical of these materials, resulting in an absorption tail at an energy lower than the band gap one (Urbach tail), which complicates the accurate extraction of the optical band gap energy. At any rate, the obtained values are broadly in line with what is expected for kesterites. [38,39].

The powders of the annealed samples were measured in reflectance mode and compared with the raw samples measured in the same conditions. A slight increase in the E_g values is observed for the annealed samples compared to those of the raw samples. Although the observed differences are slightly beyond the uncertainty of the determination and thus caution should be exerted in drawing conclusions, one can attribute this behaviour to two main factors: (i) enhanced cationic ordering on annealing and (ii) chemical non-homogeneity and secondary phase formation. The first hypothesis is supported by the fact that high temperature facilitates the movement of cations, promoting the ordering and crystallinity of the samples, confirmed by XRD and Raman analyses. [40,41] Conversely, concerning the second hypothesis, the samples exhibited non-homogeneous distribution of Cu and Zn cations,

confirmed by STEM analyses. Such compositions often result in the formation of Cu-poor secondary phases ZnS or SnS or induce intrinsic structural defects that can modify the electronic structure, and thus the effective E_g. [42] The presence of SnS secondary phases is also in agreement with XRD characterization (see previous section). Band gap values in the range 1.07–1.5 eV [43] are typically reported for SnS.

3.2. Continuous wave electron paramagnetic resonance

cw-EPR spectroscopy is a well-suited technique for the identification of paramagnetic impurities in solid state systems. [44] Despite these features, it has not been much used in the characterization of kesterites, with a few notable exceptions. [26,45–47] In the present study, this technique may provide useful insight on the presence of point defects and defect clusters, which can have a direct impact on materials performances. Consequently, we collected powder X-band ($h\nu \approx 9.4$ GHz) EPR spectra on all samples across a range of temperatures from 5 K up to room temperature (Fig. 5). Starting from the spectra of CZTS reported in Fig. 5a, a composite and partially anisotropic signal at $g \approx 2.15$ is visible in the whole temperature range and is compatible with Copper(II) species. [48] This is consistent with recent reports on nanocrystalline kesterites, which showed evidence of a small fraction of Copper(II) in EPR spectra, despite the corresponding XPS spectra being dominated by Copper(I) signal [46] and of two different Copper(II) related signals due to both the secondary Cu_xS phase and to a paramagnetic impurity. [45] The spectrum at 5 K was consistently simulated [22] by assuming two different contributions arising from S=1/2 species (Fig. S5): the first one with an anisotropic Zeeman and hyperfine interactions to Cu nuclei, and the second one with an isotropic $g=2.17 \pm 0.01$ (see Table S3 in Supplementary Information for the complete set of parameters).

While the former species can be attributed to a residual Copper(II) impurity, with the metal ion in a tetragonally elongated environment, the second one is compatible with the EPR spectrum of Cu^{2+} clusters previously detected in kesterite samples. [26] Interestingly, thermal annealing at 450 °C strongly affects the spectra (Fig. 5b); indeed, the spectrum of a-CZTS sample is dominated by a narrow signal close to g=2 and by a broad, low-field feature which shifts to a lower field on decreasing temperature. A more detailed analysis of the region around g=2 further evidences the presence of an anisotropic structured signal at $g \sim 2.15$. Accordingly, the central region of the spectrum was simulated (see Fig. S6 and Table S3) by considering three different S=1/2 contributions: a narrow, isotropic signal centered at $g = 2.0005 \pm 0.0003$, a second broad isotropic signal centered at $g = 2.16 \pm 0.01$, and a third, anisotropic contribution ($g_{x,y} = 2.055 \pm 0.002$ and $g_z = 2.290 \pm 0.005$). The narrow isotropic signal is strongly suggestive of the formation of paramagnetic vacancies in the lattice, as recently reported for nanostructured CZTS developed for CO_2 photoreduction catalysis, [49] while the isotropic broad signal is essentially the same observed in the non-annealed samples. In particular, the observed g-values for the narrow isotropic signal are in principle compatible with different possibilities, ranging from the formation of sulfur vacancies [49,50] to the formation of defect states associated with SnS secondary phases. [51].

On the other hand, the variation of the principal g values of the anisotropic signal upon annealing points to a change in the coordination environment of the Copper(II) tetragonal impurity. Finally, the broad, temperature-shifting signal is typical of clustered systems, resulting from annealing-induced aggregation. [52,53].

The low-temperature EPR spectrum of the CZFTS sample (Fig. 5c) is dominated by three main signals: i) a partially anisotropic one at $g_{eff} \approx 4.27$, which is a common occurrence for Iron(III) species with a large zero field splitting in rhombic symmetry [48]; ii) a low-field shoulder; iii) an anisotropic contribution with hyperfine structure, much

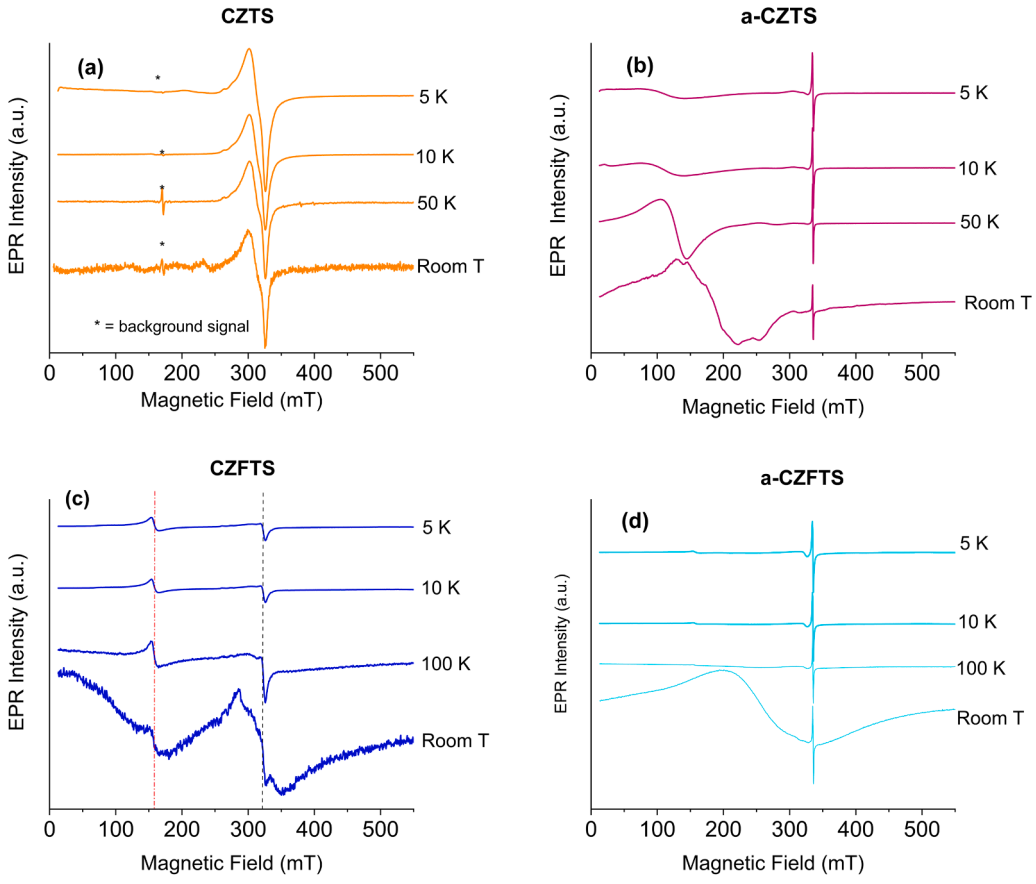

Fig. 5. X-band EPR spectra of the four microcrystalline powder samples as a function of temperature: (a) CZTS; (b) a-CZTS; (c) CZFTS; (d) a-CZFTS.

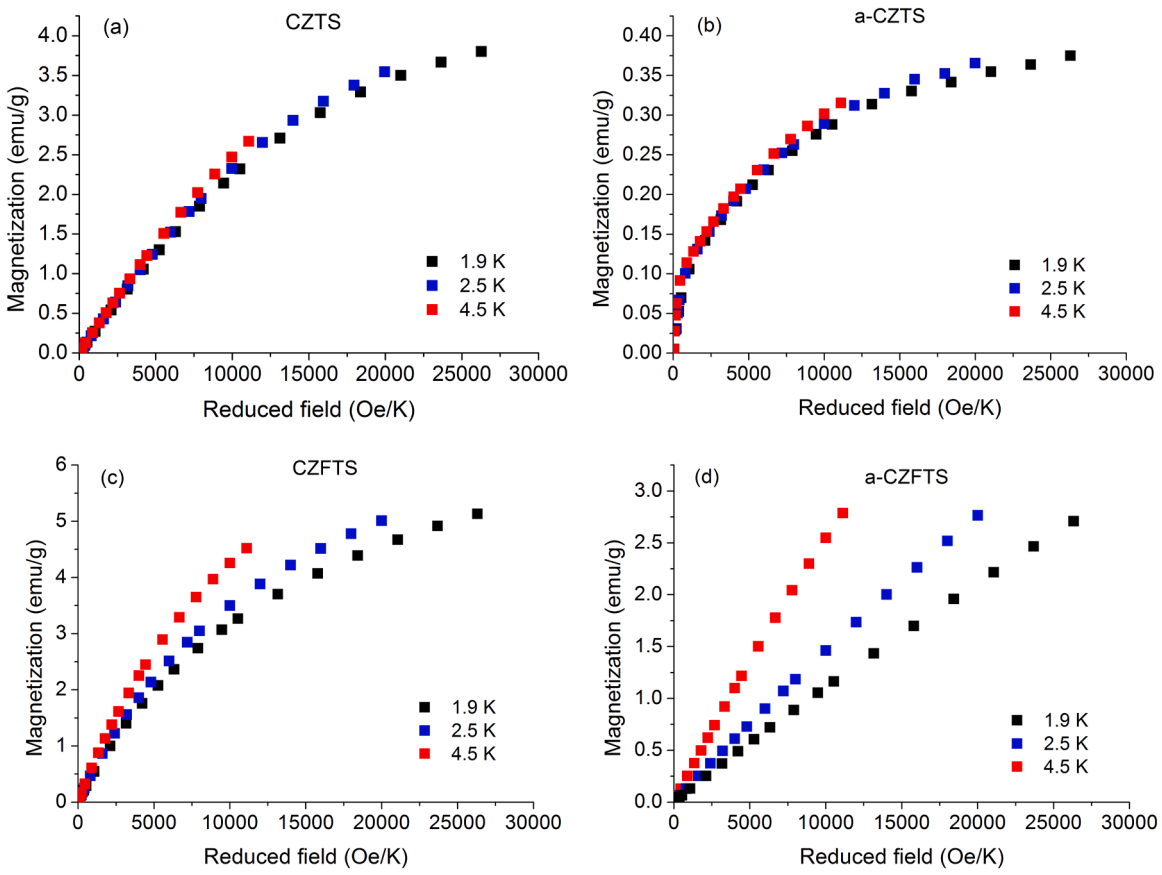

Fig. 6. Magnetization per mass vs reduced field measured at three different temperatures, for the four samples investigated: a) CZTS; (b) a-CZTS; (c) CZFTS; (d) a- CZFTS.

resembling the one observed for CZTS. Accordingly, the spectrum acquired at 5 K was simulated (see Fig. S7 and Table S3) by considering two different species: an S=5/2 with large zero field splitting parameter (*D*) and high rhombicity (*E/D*), and an S=1/2 with anisotropic g and hyperfine coupling tensor. To account for the anisotropic shape of the g ≈ 4.27 signal, which would otherwise be isotropic for a purely rhombic system, [48] we assumed a gaussian distribution in its rhombicity parameter, centered at *E/D*=0.285. Interestingly, the observed spectrum, and the corresponding simulation parameters, bears a strong similarity with the one of rubredoxin, characterized by a FeS_4 chromophore in a distorted tetrahedral environment. [54] On increasing temperature, a broad signal centered around g=2.00 appears, suggesting that the system contains clusters that, on the basis of the resonant field value, are possibly made of Iron(III). [52,53].

Also in this case, thermal annealing produces a drastic change in the spectrum (Fig. 5d). As reported above for the a-CZTS, a narrow signal centered at g=2.00 is evident in the spectrum of a-CZFTS, indicating the formation of paramagnetic centers in the lattice on heating. This suggests that the loss of Sulfur results from the annealing in a pure inert atmosphere, independently from the presence of Iron. At the same time, at T = 5 K the Iron(III) signal at g ≈ 4.27 and the anisotropic Copper(II) ones ($g_{x,y}$ = 2.08, g_z= 2.39) are strongly reduced in intensity (see Fig. S8 and Table S3 for the simulation parameters) and a broad signal becomes evident at T = 300 K. Its behavior is typical for large aggregates of Iron (III) [52,53], which we consider can form upon thermal treatment.

3.3. Magnetic properties

The results of the magnetic analysis carried out on the four samples are reported in Fig. 6, where the magnetization M is displayed as a function of the reduced field H/T, and in Fig. 7, which shows the thermal dependence of M in an applied field of H = 10 kOe, and the corresponding 1/ χ vs. T curves, being χ the mass magnetic susceptibility obtained as M/H. In the case of CZTS, the curves of M vs. reduced field are superimposed (Fig. 6a) and the trend of 1/χ vs. T is linear in a large temperature interval (Fig. 7a). These findings indicate that this sample behaves as a paramagnet, as some of us already reported. [45] This behavior is attributed to Copper(II) centers. To check that, and also to evaluate the Copper(II) fraction, relative to the total amount of Copper, we compared the experimental M vs. H curves, at T = 1.9, 2.5 and 4.5 K, with Brillouin functions corresponding to g = 2.15, as per EPR data (Fig. S9). Assuming that the sample formula is Cu_2ZnSnS_4, we obtained that the Copper(II) fraction is ~ 30% per mole of kesterite (i.e., 15% of the total Copper is in +2 oxidation state).

In a-CZTS, M vs. H/T curves are superimposed but a sharp increase in M is observed at very low values of the reduced field (Fig. 6b, detailed view in Fig. S10), which reaches ~0.1 emu/g at 2 kOe. Interestingly, the M vs. T curve shows the presence of a nearly constant background signal at essentially the same value of ~0.1 emu/g, which is reflected in the strong deviation from linearity of the corresponding 1/χ curve (Fig. 7b). These findings support the existence in a-CZTS of a fast-saturating magnetization contribution, which shows a weak thermal dependence in the investigated temperature range. We tentatively attribute this to the thermally induced formation of a component with ferromagnetic-type ordering, which is the same giving the temperature-shifting signal in EPR (Fig. 5b). The remaining part of the sample is much less magnetic than CZTS. In fact, the magnetization values M_{max} measured in a-CZTS at the highest reduced field (namely at an applied field H = 50 kOe, at three different temperatures), to which the component with ferromagnetic-type ordering contributes about 25%, are one order of

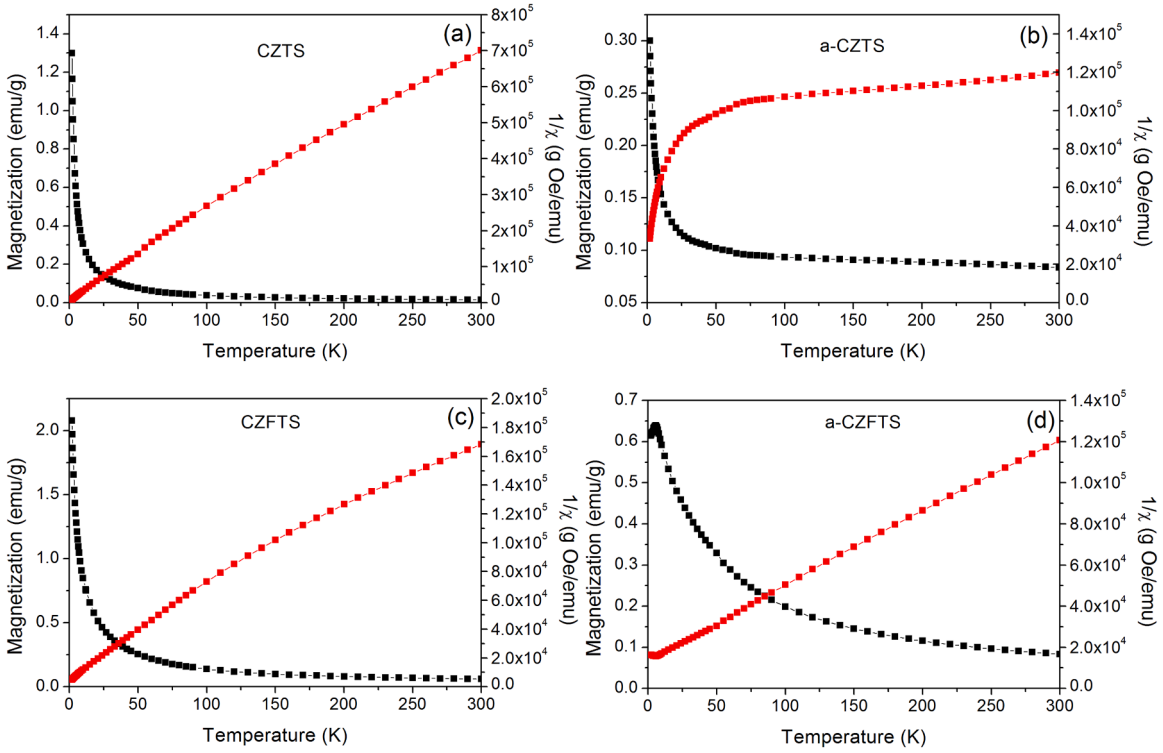

Fig. 7. Magnetization per mass (full black squares) and inverse of the mass susceptibility χ as a function of temperature (empty red triangles) for sample CZTS (a), a-CZTS (b), CZFTS (c), and a-CZFTS (d).

magnitude lower than those found in CZTS (Fig. 6a-b; see also Table S4). In line with the EPR analysis of CZTS and a-CZTS, which suggests a decrease in Copper(II) abundance (Fig. S11), this result indicates that the concentration of paramagnetic species in a-CZTS is an order of magnitude lower than that present in CZTS.

As for CZFTS, the doping introduces in the sample an amount of Iron which is ~ 5 wt% resulting in an increase in M_{max} of about 35% (at 1.9 K, Fig. 6c). This is consistent with the paramagnetic nature of both species which are introduced in the material: Iron(III) (observed by EPR) and Iron(II) which, despite being usually EPR silent at X-band frequency, is known to be present. [55].

The M vs. H/T curves in Fig. 6c are not superimposed and the M vs. T curve shows a small temperature independent contribution of ~0.06 emu/g, resulting in a slight deviation from linearity in the trend of 1/χ vs. T (Fig. 7c). Overall, these results indicate that the magnetic state of the material could not be described as purely paramagnetic - in line with the presence of a relevant anisotropy, which is tentatively attributed to the magnetocrystalline anisotropy of both Iron(II) and Iron (III) centers - and that clusters with some degree of magnetic order developed into the sample, as already inferred from the room temperature EPR analysis (Fig. 5c).

In a-CZFTS, the M vs. H/T curves do not superimpose and display a linear trend (Fig. 6d). This finding, and the observation of a peak in the M vs. T curve at T~6 K (Fig. 7d), indicate the presence of a predominant antiferromagnetic ordering at very low temperature and the transition to a paramagnetic regime, respectively. This is consistent with the behavior reported for synthetic microcrystalline stannite, where an antiferromagnetic/paramagnetic transition was observed at 6.1 K. [55] However, we also measured a non-zero thermoremanent magnetization below T ~ 8 K (Fig. S12), indicating that the antiferromagnetic phase is not fully compensated.

Finally, the constant background in the M vs. T curve (Fig. 7d), similar to that observed in the as-prepared sample (Fig. 7c), confirms the existence of particles with a collective magnetic behavior, which is not essentially modified by the annealing treatment. Indeed, in this sample, due to the coexistence of these diverse magnetic regimes and phases, it is virtually impossible to disentangle and identify them using volume-sensitive SQUID magnetometry.

4. Discussion

The main results obtained during this study point to some general evidence. On one side magnetic measurements and EPR spectroscopy suggest a complex arrangement of valence states for both Copper and Iron, in raw and thermally annealed samples. On the other one, the determination of the phase composition by XRD, Raman, and UV-Vis analyses yields a comparatively simpler picture: raw samples show monophasic kesterite phases which are only moderately affected by the thermal annealing, resulting in a crystallite evolution and in the partial segregation of a SnS phase. The two sets of information taken together evidence that the materials investigated present different levels of complexity. Thus, the integration of structural characterization methods such as XRD and vibrational spectroscopies with other ones, able to unravel the nature of valence states, is very useful to compare different materials composition and more subtle features.

CZTS is obtained starting from Copper(II), Zinc(II) and Tin(IV) precursors: considering that the formal valence states of the metal ions in CZTS are Copper(I), Zinc(II) and Tin(IV), the synthetic process must accomplish the reduction of Copper(II) while also providing the structural arrangement to accommodate the larger Copper(I). The reduction step can be driven even by the solvent, according to [45]: however, the presence of Copper(II) in the product, highlighted by EPR, suggests that the reduction process is incomplete. This might be caused either by the mild temperature of synthesis, the presence of Cu_{Zn} antisite defects, or by the reaction pathway mainly falling in the nucleation regime. A fraction of ions in unexpected valence states (i.e. Copper(II) and Iron (III)) is also observed in the raw CZFTS sample. In this case it is important to recognize that in most natural and synthetic Cu-,

Fe-bearing sulfides (both ternary and multinary) the presence of Iron (III) is frequently observed. This has been attributed to an internal redox re-balance, the couple Copper(I)/Iron(III) being more favored under sulfidic environment than the Copper(II)/Iron(II) one, [56–58] a process which we suggest occurs also in our case. The inhomogeneous cation distribution observed by the STEM investigation in both samples can also be traced back to the same process.

In general, one can state that in the raw CZTS and CZFTS samples the structural arrangement is very close to the expected model, whereas the samples are in a metastable state in terms of metal valence state and cation distribution. The annealing thus promotes an evolution of the raw samples towards the most stable valence states in the system, i.e. Copper (I) and Iron(II), as testified by the quenching of magnetization. This process, however, is not the only one occurring on annealing. At least three other concurrent processes are worth mentioning:

1) The rearrangement (migration) towards a more ordered and thermodynamically stable configuration of the metal cations in the lattice, as suggested by the magnetic data.
2) The evolution towards a thermodynamically more stable phase composition, as indicated by the occurrence of herzenbergite in both the annealed samples (albeit the amount of the secondary phase in the doped annealed sample is close to the minimum detection limit of the measurement). Thus, while the system evolves towards a more stable and ordered configuration, accessory phases can be formed at the expenses of the pristine kesterite phase due to their intrinsic higher stability. [24,28,29,59]
3) The formation of paramagnetic defects, as evidenced by EPR spectroscopy.

5. Conclusions

The results reported here evidence the importance of a multi-technique structural and magnetic analysis of polycrystalline CZTS NCs and, more generally, of nanocrystalline functional materials, to obtain an accurate structural, chemical and electronic description of these systems. We demonstrated that a combination of XRD/Raman and magnetic measurements/EPR spectroscopy significantly improves our ability to identify the formation of secondary phases, even in small amounts, and the assignment of valence states and defect formation. As for the main properties of the synthesized samples, doping of CZTS with Iron resulted in a widespread distribution within the nanoparticles and accumulation in regions corresponding to the CZTS phase, where at least a part of the total Fe replaces Zn atoms. This is complemented by EPR analysis which unequivocally proves that part of the Iron is in the +3-oxidation state and indicates the formation of a nanostructured clustered phase.

Both for doped and undoped samples, thermal annealing improves, as expected, the crystallinity of nanoparticles, thus enabling the identification of secondary phases not visible in the raw NCs. Moreover, the EPR results indicate that, in absence of a sulfur source, the thermal treatment induces a mechanical and morphological degradation of the CZTS lattice and favors the occurrence of magnetically-active complex defects, which may reduce the efficiency of CZTS as an absorber material. [15] As a future perspective, we suggest that the multi-technique approach reported here can be applied to different batch of kesterite nanoparticles in parallel with optoelectronic characterization of their devices. This would allow one to correlate paramagnetic defects formation with photovoltaic performance of the device, finally enabling to guide material synthesis toward improved efficiency.

CRediT authorship contribution statement

Giulia Millacci: Writing – original draft, Investigation, Formal analysis, Data curation. **Alessandro Veneri:** Writing – review & editing, Writing – original draft, Supervision, Methodology, Investigation, Conceptualization. **Andrea Dali:** Writing – review & editing, Writing – original draft, Investigation, Formal analysis, Data curation. **Alessio Gabbani:** Writing – review & editing, Writing – original draft, Supervision, Investigation, Data curation, Conceptualization. **Beatrice Muzzi:** Writing – review & editing, Writing – original draft, Investigation, Formal analysis, Data curation. **Federico Spizzo:** Writing – review & editing, Writing – original draft, Visualization, Investigation, Formal analysis, Data curation. **Arianna Rossi:** Writing – review & editing, Investigation, Data curation. **Matteo Mannini:** Writing – review & editing, Supervision, Resources, Funding acquisition, Conceptualization. **Maurizio Becucci:** Writing – review & editing, Writing – original draft, Resources, Investigation, Formal analysis. **Lucia Del Bianco:** Writing – review & editing, Supervision, Resources, Methodology, Formal analysis. **Francesco Pineider:** Writing – review & editing, Supervision, Project administration. **Francesco Di Benedetto:** Writing – review & editing, Writing – original draft, Project administration, Funding acquisition, Formal analysis, Conceptualization. **Lorenzo Sorace:** Writing – review & editing, Writing – original draft, Supervision, Project administration, Funding acquisition, Formal analysis.

Declaration of Competing Interest

The authors declare that they have no known competing financial interests or personal relationships that could have appeared to influence the work reported in this paper.

Acknowledgments

This work was financially supported by MUR through PRIN2022PNRR project P20229723Z (CUP: B53D23025560001). A.V. and M.M. gratefully acknowledge MUR and EU-FSE for the financial support of the PhD fellowship PON Research and Innovation 2014–2020 (D.M. 1061/2021) and GEA Green Economy and Agriculture Centro per la Ricerca s.r.l. The personnel of the Centre for Structural Crystallography (CRIST UNIFI) and of the Interdepartmental Research Unit Matchlab (N. Calisi and B. Cortigiani) are gratefully acknowledged for technical support. Authors thank the COST Action CA21148 “Research and International Networking on Emerging Inorganic Chalcogenides for Photovoltaics (RENEW-PV)”.

Supplementary data

Supplementary information contains simulation of PXRD patterns obtained by Rietveld refinement and of EPR spectra, as well as tabulated Spin Hamiltonian parameters of best simulated spectra and magnetization values at 50 KOe at different temperatures.

Appendix A. Supporting information

Supplementary data associated with this article can be found in the online version at doi:10.1016/j.materresbull.2026.114253.

Data availability

Data will be made available on request.

References

[1] A.J. Jackson, A. Walsh, Ab initio thermodynamic model of Cu_2ZnSnS_4, J. Mater. Chem. A. 2 (2014) 7829–7836, https://doi.org/10.1039/C4TA00892H.
[2] M.Y. Zaki, A. Velea, Recent Progress and Challenges in Controlling Secondary Phases in Kesterite CZT(S/Se) Thin Films: A Critical Review, Energies 17 (2024) 1600, https://doi.org/10.3390/en17071600.
[3] M.A. Olgar, Optimization of sulfurization time and temperature for fabrication of Cu_2ZnSnS_4 (CZTS) thin films, Superlattices Microstruct. 126 (2019) 32–41, https://doi.org/10.1016/j.spmi.2018.12.012.
[4] E. Indubala, S. Sarveshvaran, V. Sudha, A.Y. Mamajiwala, S. Harinipriya, Secondary phases and temperature effect on the synthesis and sulfurization of

CZTS, Sol. Energy 173 (2018) 215–224, https://doi.org/10.1016/j.solener.2018.07.085.
[5] K. Pal, P. Singh, A. Bhaduri, K.B. Thapa, Current challenges and future prospects for a highly efficient (>20%) kesterite CZTS solar cell: A review, Sol. Energy Mater. Sol. Cells 196 (2019) 138–156, https://doi.org/10.1016/j.solmat.2019.03.001.
[6] W.-C. Hsu, H. Zhou, S. Luo, T.-B. Song, Y.-T. Hsieh, H.-S. Duan, S. Ye, W. Yang, C.-J. Hsu, C. Jiang, B. Bob, Y. Yang, Spatial element distribution control in a fully solution-processed nanocrystals-based 8.6% $Cu_2ZnSn(S,Se)_4$ device, ACS Nano 8 (2014) 9164–9172, https://doi.org/10.1021/nn503992e.
[7] J. Just, C.M. Sutter-Fella, D. Lützenkirchen-Hecht, R. Frahm, S. Schorr, T. Unold, Secondary phases and their influence on the composition of the kesterite phase in CZTS and CZTSe thin films, Phys. Chem. Chem. Phys. 18 (2016) 15988–15994, https://doi.org/10.1039/C6CP00178E.
[8] R. Paul, S. Shukla, T.R. Lenka, F.A. Talukdar, V. Goyal, N.E.I. Boukortt, P.S. Menon, Recent progress in CZTS (CuZnSn sulfide) thin-film solar cells: a review, J. Mater. Sci. Mater. Electron. 35 (2024) 226, https://doi.org/10.1007/s10854-024-11983-0.
[9] U.A. Shah, A. Wang, M. Irfan Ullah, M. Ishaq, I.A. Shah, Y. Zeng, M.S. Abbasi, M. A. Umair, U. Farooq, G.-X. Liang, K. Sun, A deep dive into Cu_2ZnSnS_4 (CZTS) solar cells: a review of exploring roadblocks, breakthroughs, and shaping the future, Small 20 (2024) 2310584, https://doi.org/10.1002/smll.202310584.
[10] R. Massadeh, M.M. Hamasha, Comprehensive review of CZTS deposition techniques and experimental insights into low-temperature chemical synthesis of CZTS thin film solar cells, Opt. Mater. (Amst.). 157 (2024) 116427, https://doi.org/10.1016/j.optmat.2024.116427.
[11] L. Sravani, S. Routray, M. Courel, K.P. Pradhan, Loss mechanisms in CZTS and CZTSe Kesterite thin-film solar cells: Understanding the complexity of defect density, Sol. Energy 227 (2021) 56–66, https://doi.org/10.1016/j.solener.2021.08.052.
[12] C. Sripan, V.E. Madhavan, A.K. Viswanath, R. Ganesan, Sulfurization and annealing effects on thermally evaporated CZTS films, Mater. Lett. 189 (2017) 110–113, https://doi.org/10.1016/j.matlet.2016.11.094.
[13] S. Engberg, F. Martinho, M. Gansukh, A. Protti, R. Küngas, E. Stamate, O. Hansen, S. Canulescu, J. Schou, Spin-coated Cu_2ZnSnS_4 solar cells: A study on the transformation from ink to film, Sci. Rep. 10 (2020) 20749, https://doi.org/10.1038/S41598-020-77592-Z.
[14] Y. Qu, G. Zoppi, R.W. Miles, N.S. Beattie, Influence of reaction conditions on the properties of solution-processed Cu_2ZnSnS_4 nanocrystals, Mater. Res. Express 1 (2014) 045040, https://doi.org/10.1088/2053-1591/1/4/045040.
[15] S. Kim, J.S. Park, A. Walsh, Identification of Killer Defects in Kesterite Thin-Film Solar Cells, ACS Energy Lett. 3 (2018) 496–500, https://doi.org/10.1021/ACSENERGYLETT.7B01313.
[16] Y. Wang, R. Hao, J. Guo, X. Li, S. Fang, H. Liu, S. Sun, Effect of Mg doping on Cu_2ZnSnS_4 solar cells prepared by DMF-based solution method, Opt. Mater. (Amst.). 117 (2021) 111211, https://doi.org/10.1016/J.OPTMAT.2021.111211.
[17] J. Rodríguez-Carvajal, Recent Developments of the Program FULLPROF, Comm. Powder Diffr. Newsl. 26 (2001) 12–19.
[18] Y.A. Romaniuk, I.S. Babichuk, V.V. Korotyeyev, V.O. Yukhymchuk, V.M. Dzhagan, S.V. Virko, M.O. Semenenko, M.O. Stetsenko, A. Tiutiunnyk, L.M. Pérez, D. Laroze, Influence of phonon anharmonicity on Raman spectra of $Cu_2ZnSn(S,Se)_4$ polycrystalline thin films through computational study, Sci. Rep. 15 (2025) 366, https://doi.org/10.1038/s41598-024-83117-9.
[19] M. Wojdyr, Fityk: a general-purpose peak fitting program, UrnIssn0021-8898 43 (2010) 1126–1128, https://doi.org/10.1107/S0021889810030499.
[20] X. Fontané, V. Izquierdo-Roca, E. Saucedo, S. Schorr, V.O. Yukhymchuk, M. Y. Valakh, A. Pérez-Rodríguez, J.R. Morante, Vibrational properties of stannite and kesterite type compounds: Raman scattering analysis of $Cu_2(Fe,Zn)SnS_4$, J. Alloy. Compd. 539 (2012) 190–194, https://doi.org/10.1016/j.jallcom.2012.06.042.
[21] M. Dimitrievska, A. Fairbrother, X. Fontané, T. Jawhari, V. Izquierdo-Roca, E. Saucedo, A. Pérez-Rodríguez, Multiwavelength excitation Raman scattering study of polycrystalline kesterite Cu_2ZnSnS_4 thin films, Appl. Phys. Lett. 104 (2014), https://doi.org/10.1063/1.4861593.
[22] S. Stoll, A. Schweiger, EasySpin, a comprehensive software package for spectral simulation and analysis in EPR, J. Magn. Reson. 178 (2006) 42–55, https://doi.org/10.1016/j.jmr.2005.08.013.
[23] G.A. Bain, J.F. Berry, Diamagnetic Corrections and Pascal's Constants, J. Chem. Educ. 85 (2008) 532, https://doi.org/10.1021/ed085p532.
[24] G. Montegrossi, F. Meloni, A. Giaccherini, A. Veneri, M. Ardit, M. Mannini, F. Di Benedetto, Aqueous phase stability of multinary thiostannates, Appl. Geochem. 191 (2025) 106513, https://doi.org/10.1016/J.APGEOCHEM.2025.106513.
[25] G.P. Bernardini, P. Bonazzi, M. Corazza, F. Corsini, G. Mazzetti, L. Poggi, G. Tanelli, New data on the Cu_2FeSnS_4-Cu_2ZnSnS_4 pseudobinary system at 750 ° and 550 ° C, Eur. J. Mineral. 2 (1990) 219–225.
[26] G.P. Bernardini, D. Borrini, A. Caneschi, F. Di Benedetto, D. Gatteschi, S. Ristori, M. Romanelli, EPR and SQUID magnetometry study of Cu_2FeSnS_4 (stannite) and Cu_2ZnSnS_4 (kesterite), Phys. Chem. Miner. 27 (2000) 453–461, https://doi.org/10.1007/S002690000086.
[27] M. Kumar, A. Dubey, N. Adhikari, S. Venkatesan, Q. Qiao, Strategic review of secondary phases, defects and defect-complexes in kesterite CZTS–Se solar cells, Energy Environ. Sci. 8 (2015) 3134–3159, https://doi.org/10.1039/C5EE02153G.
[28] A. Weber, R. Mainz, H.W. Schock, On the Sn loss from thin films of the material system Cu-Zn-Sn-S in high vacuum, J. Appl. Phys. 107 (2010) 13516, https://doi.org/10.1063/1.3273495/287403.
[29] J.J. Scragg, T. Ericson, T. Kubart, M. Edoff, C. Platzer-Björkman, Chemical insights into the instability of cu2znsns4 films during annealing, Chem. Mater. 23 (2011) 4625–4633, https://doi.org/10.1021/CM202379S.
[30] P. Bonazzi, L. Bindi, G.P. Bernardini, S. Menchetti, A model for the mechanism of incorporation of Cu, Fe and Zn in the stannite-kesterite series, Cu_2FeSnS_4 – Cu2ZnSnS4, Can. Mineral. 41 (2003) 639–647, https://doi.org/10.2113/gscanmin.41.3.639.
[31] S. Schorr, The crystal structure of kesterite type compounds: A neutron and X-ray diffraction study, Sol. Energy Mater. Sol. Cells 95 (2011) 1482–1488, https://doi.org/10.1016/J.SOLMAT.2011.01.002.
[32] R.W.G. Wyckoff, Crystal Structures, Interscience Publisher,, New York, 1963.
[33] ⟨https://rruff.info/kesterite⟩, (n.d.). https://rruff.info/kesterite.
[34] X. Fontané, L. Calvo-Barrio, V. Izquierdo-Roca, E. Saucedo, A. Prez-Rodriguez, J. R. Morante, D.M. Berg, P.J. Dale, S. Siebentritt, In-depth resolved Raman scattering analysis for the identification of secondary phases: Characterization of Cu_2ZnSnS_4 layers for solar cell applications, Appl. Phys. Lett. 98 (2011) 181905, https://doi.org/10.1063/1.3587614.
[35] A.-J. Cheng, M. Manno, A. Khare, C. Leighton, S.A. Campbell, E.S. Aydil, Imaging and phase identification of Cu_2ZnSnS_4 thin films using confocal Raman spectroscopy, J. Vac. Sci. Technol. A. 29 (2011), https://doi.org/10.1116/1.3625249.
[36] P.A. Fernandes, P.M.P. Salomé, A.F. Da Cunha, Study of polycrystalline Cu_2ZnSnS_4 films by Raman scattering, J. Alloy. Compd. 509 (2011) 7600–7606, https://doi.org/10.1016/J.JALLCOM.2011.04.097.
[37] B. Muzzi, E. Lottini, N. Yaacoub, D. Peddis, G. Bertoni, C. De Julián Fernández, C. Sangregorio, A. López-Ortega, Hardening of Cobalt Ferrite Nanoparticles by Local Crystal Strain Release: Implications for Rare Earth Free Magnets, ACS Appl. Nano Mater. 5 (2022) 14871–14881, https://doi.org/10.1021/ACSANM.2C03161.
[38] X. Zhang, N. Bao, K. Ramasamy, Y.H.A. Wang, Y. Wang, B. Lin, A. Gupta, Crystal phase-controlled synthesis of Cu_2FeSnS_4 nanocrystals with a band gap of around 1.5 eV, Chem. Commun. 48 (2012) 4956–4958, https://doi.org/10.1039/c2cc31648j.
[39] C. Malerba, F. Biccari, C.L.A. Ricardo, M. Valentini, R. Chierchia, M. Müller, A. Santoni, E. Esposito, P. Mangiapane, P. Scardi, A. Mittiga, CZTS stoichiometry effects on the band gap energy, J. Alloy. Compd. 582 (2014) 528–534, https://doi.org/10.1016/j.jallcom.2013.07.199.
[40] C. Krämmer, C. Huber, C. Zimmermann, M. Lang, T. Schnabel, T. Abzieher, E. Ahlswede, H. Kalt, M. Hetterich, Reversible order-disorder related band gap changes in $Cu_2ZnSn(S,Se)_4$ via post-annealing of solar cells measured by electroreflectance, Appl. Phys. Lett. 105 (2014), https://doi.org/10.1063/1.4905351.
[41] J.K. Larsen, J.J.S. Scragg, N. Ross, C. Platzer-Björkman, Band tails and Cu–Zn disorder in Cu_2ZnSnS_4 solar cells, ACS Appl. Energy Mater. 3 (2020) 7520–7526, https://doi.org/10.1021/acsaem.0c00926.
[42] M. Kauk-Kuusik, K. Timmo, K. Muska, M. Pilvet, J. Krustok, R. Josepson, G. Brammertz, B. Vermang, M. Danilson, M. Grossberg, Detailed Insight into the CZTS/CdS Interface Modification by Air Annealing in Monograin Layer Solar Cells, ACS Appl. Energy Mater. 4 (2021) 12374–12382, https://doi.org/10.1021/acsaem.1c02186.
[43] F. Kawamura, Y. Song, H. Murata, H. Tampo, T. Nagai, T. Koida, M. Imura, N. Yamada, Tunability of the bandgap of SnS by variation of the cell volume by alloying with A.E. elements, 2022 121, Sci. Rep. 12 (2022) 7434, https://doi.org/10.1038/s41598-022-11074-2.
[44] E. Giamello, M. Chiesa, M.C. Paganini, Point Defects in Electron Paramagnetic Resonance, Springer Ser. Surf. Sci. 58 (2015) 303–326, https://doi.org/10.1007/978-3-319-14367-5_10.
[45] A. Veneri, A. Privitera, A. Gabbani, B. Muzzi, M. Becucci, A. Caneschi, F. Di Benedetto, F. Pineider, L. Sorace, M. Mannini, Environmentally Friendly Pathway to Kesterite Nanoparticles with Controlled Sn Content: An In-Depth Study of Magnetic and Optical Properties, J. Phys. Chem. C. 128 (2024) 10903–10914, https://doi.org/10.1021/ACS.JPCC.4C02095.
[46] I. Vorona, V. Dzhagan, V. Nosenko, S. Kondratenko, O. Selyshchev, M. Valakh, S. Okulov, N. Mazur, O. Raievska, O.L. Stroyuk, D.R.T. Zahn, Room-Temperature Electron Paramagnetic Resonance Study of a Copper-Related Defect in Cu2ZnSnS4Colloidal Nanocrystals, J. Phys. Chem. C. 125 (2021) 9923–9929, https://doi.org/10.1021/ACS.JPCC.1C02176.
[47] C. Chory, F. Zutz, F. Witt, H. Borchert, J. Parisi, Synthesis and characterization of Cu_2ZnSnS_4, Phys. Status Solidi C. 7 (2010) 1486–1488, https://doi.org/10.1002/PSSC.200983217.
[48] J.R. Pilbrow, Transition Ion Electron Paramagnetic Resonance, Clarendon Press,, Oxford, UK, 1990.
[49] X. Li, L. Li, X. Liu, J. Xu, X. Chu, G. Chen, D. Li, M. Wang, X. Wang, C. Naisa, J. Gao, Y. Sun, M. Grätzel, X. Feng, Designing multi-metal-site nanosheet catalysts for CO_2 photoreduction to ethylene, Nat. Commun. 16 (2025) 6500, https://doi.org/10.1038/s41467-025-61850-7.
[50] S. Hu, X. Chen, Q. Li, Y. Zhao, W. Mao, Effect of sulfur vacancies on the nitrogen photofixation performance of ternary metal sulfide photocatalysts, Catal. Sci. Technol. 6 (2016) 5884–5890, https://doi.org/10.1039/C6CY00622A.
[51] A.M. Panich, A.I. Shames, R.E. Abutbul, N. Maman, S.D. Goren, Y. Golan, NMR and EPR study of cubic π-phase SnS semiconductor nanoparticles, Mater. Chem. Phys. 250 (2020) 123206, https://doi.org/10.1016/J.MATCHEMPHYS.2020.123206.
[52] C. Carbone, F. Di Benedetto, P. Marescotti, C. Sangregorio, L. Sorace, N. Lima, M. Romanelli, G. Lucchetti, C. Cipriani, Natural Fe-oxide and -oxyhydroxide nanoparticles: an EPR and SQUID investigation, Mineral. Petrol. 85 (2005) 19–32, https://doi.org/10.1007/s00710-005-0098-0.
[53] M. Fittipaldi, L. Sorace, A. Barra, C. Sangregorio, R. Sessoli, D. Gatteschi, Molecular nanomagnets and magnetic nanoparticles: the EMR contribution to a common approach, Phys. Chem. Chem. Phys. 11 (2009) 6555–6568, https://doi.org/10.1039/B905880J.

[54] J. Peisach, W.E. Blumberg, E.T. Lode, M.J. Coon, An Analysis of the Electron Paramagnetic Resonance Spectrum of Pseudomonas oleovorans Rubredoxin: a method for determination of the ligands of ferric iron in completely rhombic sites, J. Biol. Chem. 246 (1971) 5877–5881, https://doi.org/10.1016/S0021-9258(18)61807-1.

[55] A. Caneschi, C. Cipriani, F.Di Benedetto, R. Sessoli, Characterisation of the antiferromagnetic transition of Cu_2FeSnS_4, the synthetic analogue of stannite, Phys. Chem. Miner. 31 (2004) 190–193, https://doi.org/10.1007/S00269-004-0381-3.

[56] K. Bente, Stabilization of Cu-Fe-Bi-Pb-Sn-sulfides, Mineral. Petrol. 36 (1987) 205–217, https://doi.org/10.1007/BF01163260.

[57] W. Zalewski, R. Bacewicz, J. Antonowicz, A. Pietnoczka, T.L. Evstigneeva, S. Schorr, XAFS study of kesterite, kuramite and stannite type alloys, J. Alloy. Compd. 492 (2010) 35–38, https://doi.org/10.1016/J.JALLCOM.2009.11.158.

[58] F. Di Benedetto, T. Evstigneeva, M. Borgheresi, A. Caneschi, M. Romanelli, The unusual magnetic properties of kuramite-stannite pseudobinary series: A SQUID and EPR survey, Phys. Chem. Miner. 36 (2009) 301–309, https://doi.org/10.1007/S00269-008-0278-7/FIGURES/8.

[59] M. Kumar, A. Dubey, N. Adhikari, S. Venkatesan, Q. Qiao, Strategic review of secondary phases, defects and defect-complexes in kesterite CZTS–Se solar cells, Energy Environ. Sci. 8 (2015) 3134–3159, https://doi.org/10.1039/C5EE02153G.